Learning the propagation properties of rectangular metal plates for Lamb wave-based mapping

Othmane-Latif Ouabi, Pascal Pomarede, Nico F Declercq, Neil Zeghidour,
Matthieu Geist, Cédric Pradalier

Learning the Propagation Properties of Rectangular Metal Plates for Lamb Wave-based Mapping⋆

Othmane-Latif Ouabi[a,∗], Pascal Pomarede[a], Nico F. Declercq[a,b], Neil Zeghidour[c], Matthieu Geist[c], Cédric Pradalier[a]

[a]*International Research Lab Georgia Tech-CNRS, 2 rue Marconi, 57070 Metz, France*
[b]*Georgia Institute of Technology, Atlanta, GA 30332-0250, USA*
[c]*Google Research, Brain Team*

Abstract

The inspection of sizeable plate-based metal structures such as storage tanks or marine vessel hulls is a significant stake in the industry, which necessitates reliable and time-efficient solutions. Although Lamb waves have been identified as a promising solution for long-range non-destructive testing, and despite the substantial progress made in autonomous navigation and environment sensing, a Lamb-wave-based robotic system for extensive structure monitoring is still lacking. Following previous work on ultrasonic Simultaneous Localization and Mapping (SLAM), we introduce a method to achieve plate geometry inference without prior knowledge of the material propagation properties, which may be lacking during a practical inspection task in challenging and outdoor environments. Our approach combines focalization to adjust the propagation model parameters and beamforming to infer the plate boundaries location by relying directly on acoustic measurements acquired along the mobile unit trajectory. For each candidate model, the focusing ability of the corresponding beamformer is assessed over high-pass filtered beamforming maps to further improve the robustness of the plate geometry estimates. We then recover the optimal space-domain beamformer through a simulated annealing optimization process. We evaluate our method on three sets of experimental data acquired in different conditions and show that accurate plate geometry inference can be achieved without any prior propagation model. Finally, the results show that the optimal beamformer outperforms the beamformer resulting from the predetermined propagation model in non-nominal acquisition conditions.

Keywords: Lamb waves, Acoustic mapping, Helmholtz equation, Optimal beamforming, Model learning

1. Introduction

During their lifetime, marine vessels are continuously deployed on the seas for goods shipping. This inexorably leads to the deterioration of the hull due, for example, to the formation of biofouling on the surface, or due to the salinity of the water that can favor the formation of defects such as cracks or corrosion patches. Other large metal structures such as storage tanks deteriorate over time due to their operational conditions, and the underpinning defects may not always be detectable with the bare eye [1]. Thus, in the marine and petrochemical industries, the inspection of large-scale metal structures – which are usually made of metal panels assembled out together – must rely on efficient solutions that can seamlessly integrate into their day-to-day operation.

Standard inspection methods are time-consuming as they often require the intervention of trained operators, causing a significant financial impact. Moreover, these methods work for localized inspection areas; thus, the entire surface cannot be inspected in a reasonable amount of time. For ship hulls inspection, for example, either human operators or robots such as magnetic crawlers [2] can apply acoustic probes on the structure surface to perform thickness measurements, and detect corrosion patches. However, only the surface directly covered by the probe is effectively controlled with a single measurement.

The inspection of structures over long ranges is being actively investigated in the literature. Lamb waves, in particular, are being integrated into modern Non Destructive Testing (NDT)-capable devices. These waves can be emitted in plate materials by piezoelectric transducers and can propagate radially over long distances in a direction parallel to the surface. What makes them appealing is that they are sensitive to material integrity. Usually, they are deployed on static networks of sensors that are permanently attached to the structure. Thus, defect detection and localization can be achieved through the triangulation of acoustic scatterers from residual signals [3, 4, 5, 6, 7], or by using baseline-free methods [8, 9, 10, 11].

Besides, the interest in the development of a robotic system for long-range inspection is steadily growing, as it

holds tremendous potential for industrial applications, and its feasibility is being demonstrated by recent works [12, 13, 14]. Yet, deploying acoustic imaging techniques on a robotic system necessitates precise localization of the transducers, which is critical for accurate inspection results. Contrary to standard Structural Health Monitoring (SHM) technology where the positions of the sensors are known accurately, these positions need to be estimated in the framework of a robotic application due to kinematics modeling errors, and due to the imprecise wheel displacement and rotation data provided by the wheels' encoders.

When induced by a source excitation, Lamb waves can reflect on the metal plate boundaries, usually without mode conversion when the excitation frequency is sufficiently appropriate [15]. As the resulting acoustic measurements contain such reflections, they provide range-only information between the source position and the plate edges which may be useful for accurate localization, in combination with other measurement systems. Lamb wave-based localization has been demonstrated for a pulse-echo setup on a rectangular and isotropic metal panel, but with prior knowledge of the structure geometry [16]. Hence, determining precisely the sensor position on a large structure is intrinsically connected to building a map of the environment (*i.e* mapping the environment) which can rapidly become a tedious task if not made automatically [17]. Furthermore, from a robotic perspective, defect detection and localization may be interpreted as a mapping problem as well. Overall, the mapping of acoustic scatterers (whether they be plate boundaries or defects) by a mobile unit is a major issue that needs to be addressed to enable the emergence of a viable robotic inspection system.

In the literature, the problem of defect detection and localization using acoustic reflections on the structure boundaries has been widely studied [18, 19, 20, 21]. Furthermore, approaches to detect the boundaries of a rectangular panel [22], to identify structural features such as stiffeners [23], or to localize an acoustic source [24, 25] have been investigated. Yet, they are deployed on static networks of sensors. A recent work [26] proposes a Lamb wave-based approach to map a rectangular metal panel using a pair of mobile sensors, along with an exploration strategy. Yet, the work is dedicated to pitch-catch configurations, the Time of Flights (ToF) readings are not done automatically, the mapping is only based on the edge echo that arrives first, and the final map may eventually be erroneous due to gridlock situations that are not predictable.

Recent works from the authors address Lamb wave based Simultaneous Localization and Mapping (SLAM), where the geometry of the plate and the position of a co-located emitter/receiver pair of piezoelectric transducers are jointly estimated. A method based on L_1-regularized Least-squares for echo detection and on a FastSLAM algorithm [27] has been presented in first instance [28]. Subsequently, propagation models to account for the dispersive nature of guided waves in metal plates and space domain Delay-And-Sum (DAS) beamforming [29] have been integrated into a FastSLAM algorithm for the exclusive mapping of rectangular shapes [30]. Results proved to be accurate on two different metal panels. However, no solutions were proposed to limit the detrimental effect of interference on the mapping results which is a well-known issue inherent to DAS beamforming [29]. Besides, the approach requires prior knowledge of the propagation model.

Prior knowledge of the physical properties of isotropic metal structures is in general sufficient for acoustic localization and mapping in well controlled environments. However, the hypothesis that the propagation model is known a priori may not be realistic for a practical inspection task on a large metal structure due to a wide variety of external perturbations that can significantly affect the acoustic signals, and to a lack of knowledge of the structure physical condition (which is the reason why it is being inspected). Potential perturbations may include but may not be limited to temperature variations which are already known to affect acoustic measurements substantially [31], pressure due to the neighboring metal plates which are welded altogether, moisture, the varying thickness of the coating, or the effect of the coupling (namely water in the case of acoustic inspection with a robotic system). Consequently, adaptive methods that automatically calibrate the propagation model by relying directly on data acquired on the field may be necessary to achieve accurate localization and mapping results, without any human intervention.

Recent works in the literature either address the problem of extracting the dispersion characteristics of materials from ultrasonic data [32, 33, 34, 35], or investigate acoustic localization techniques that can also recover the propagation properties [25, 36, 37]. However, simultaneous acoustic localization and propagation characterization from pulse-echo ultrasonic measurements acquired by a mobile unit has not been thoroughly studied. In the literature of beamforming, adaptive methods have been elaborated to compensate for inaccurate knowledge of the properties of the propagation media for underwater acoustic source localization purposes [38], or more generally, for Matched Field Processing [39]. Beamforming has been combined with focalization [40], an approach that considers the propagation environment as an acoustic lens, and which seeks, through an optimization process, to adjust the propagation parameters so that the focalization capability of beamforming is maximized. It has also been studied for joint acoustic signal separation and source localization [42]. The potential of focalization has been successfully demonstrated in simulation for underwater acoustic localization, and may provide an interesting approach for Lamb waves. Yet, this has not yet been demonstrated.

This paper proposes an approach that combines focalization and DAS beamforming to achieve Lamb wave-based mapping of a plate-like structure by a mobile unit, so that accurate mapping results can be achieved during an inspection task without prior knowledge of the propagation properties of the material. For the sake of simplicity, the localization problem is not addressed here. The proposed

approach combines focalization to adjust the parameters of propagation models that are derived from the Helmholtz equation, and beamforming to localize the plate edges. The focalization capability of a candidate beamformer is assessed over high-pass filtered beamforming maps, so that the detrimental effects of interference and high-order reflections are lowered. A simulated annealing optimization process is then implemented so that the optimal beamformer can be recovered based directly on data. Results acquired on experimental data in three different scenarios show that the proposed approach is effective. Furthermore, mapping the plate geometry with the optimal beamformer is found to be more efficient than mapping with a predetermined propagation model in non-nominal acquisition conditions.

The outline of the present article is as follows. First, the general theory on Lamb waves propagation in metal panels is briefly presented. Next, the approach based on DAS beamforming for mapping the plate edges with a single mobile platform by leveraging the acoustic reflections is recalled. The choice of the propagation parameters to search for, namely, the plate thickness, the longitudinal and transverse velocities, is then discussed, and the simulated annealing process is presented. Finally, experimental results and discussions conclude the article.

2. Lamb wave-based mapping

In what follows, we briefly recall the essential principles of the theory on Lamb waves propagation in metal plates, namely, the Rayleigh-Lamb equations. We then introduce a simple propagation model based on approximate solutions of the Helmholtz equation to account for dispersive propagation under the hypothesis of a linear model and an isotropic material. Next, we summarize the mapping strategy to localize the plate boundaries based on a known propagation model and a space-domain delay-and-sum beamformer [30]. These elements will be the basis of the core contribution of this paper, which is plate mapping without prior knowledge of the propagation model.

2.1. Lamb waves propagation in a metal plate

The theory on Lamb wave propagation in an isotropic and homogeneous wave guide is well established [41]. According to the Rayleigh-Lamb equations:

$$\frac{\tanh qh}{\tanh ph} = -\left[\frac{4k^2 qp}{(k^2 - q^2)^2}\right]^{\alpha} \tag{1}$$

where h denotes the half-thickness of the plate, $k = 2\pi/\lambda$ is the wavenumber, λ is the wavelength, and the following equations define p and q:

$$p^2 = \frac{\omega^2}{c_L^2} - k^2; \quad q^2 = \frac{\omega^2}{c_T^2} - k^2.$$

In the above equation, ω is the pulsation, and c_L and c_T are respectively the longitudinal and transverse velocities
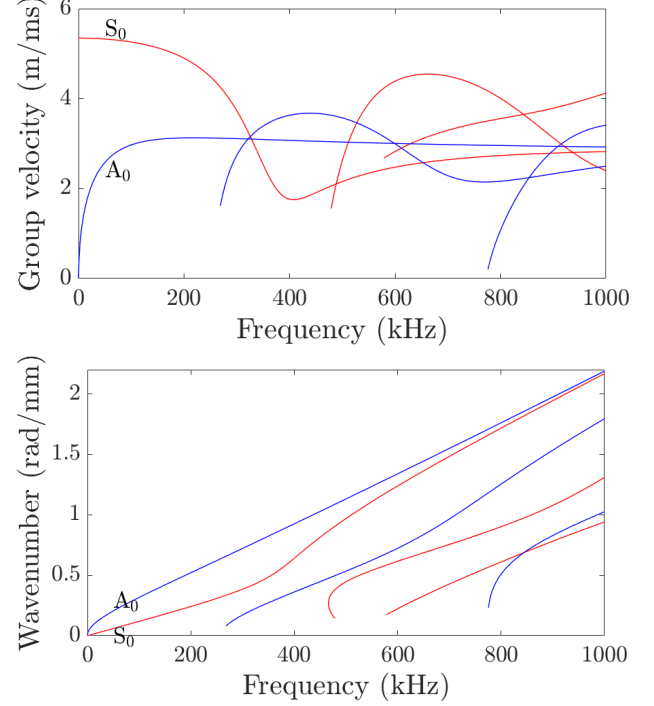

Figure 1: Dispersion curves for several low order symmetric and anti-symmetric Lamb wave modes in a 6mm thick aluminum plate. The top figure depicts the group velocities while the bottom plot shows the wavenumbers.

related to the material. For $\alpha = 1$, the equation yields the physical properties of symmetric modes, whereas for $\alpha = -1$, the properties of anti-symmetric modes are stipulated. The resolution of the equation, using dichotomy algorithms for example [3], yields a dispersion relation $k(\omega \cdot d)$ (or $k(\omega)$ for a fixed d), where $d = 2h$ is the plate thickness. One particularity is that each equation always admits at least one positive real-valued solution, and the number of solutions increases with frequency. Hence, at least the two fundamental modes A0 and S0 propagate within the material, while higher-order modes propagate when the excitation frequency exceeds their respective cutoff frequency. Fig. 1 depicts dispersion curves for symmetric and anti-symmetric modes for a 6mm thick aluminum plate. In practice, a low excitation frequency is used to avoid multi-modal propagation, and one mode is often predominant over the other fundamental mode. Also, as their velocities are frequency-dependent, these modes are dispersive, resulting in wavepacket distortion and spreading in the signal when the propagation distance increases.

Finite Element Methods (FEM) are often used to simulate Lamb waves propagation [44], but their heavy computational load makes them impractical to use for acoustic localization operations. Instead, one can rely on computationally efficient and relatively accurate propagation models given by the solutions of the Helmholtz equation, for which the wavenumber abides by the dispersion relation of the mode assumed to exist in the material. When a signal s is used to excite Lamb waves in a metal plate, under the

3

hypotheses of linear propagation and isotropic media, the vertical component u of the displacement field abides by:

$$\nabla^2 u(r, \omega) + k^2(\omega) \cdot u(r, \omega) = -s(\omega)$$

where r is the propagation distance from the excitation point. It is known that the solution, *i.e.* the acoustic transfer function $g(r, \omega)$, can be expressed with the Hankel function of 0 order and of the first kind yielding the scalar field: $u(r, \omega) = g(r, \omega) \cdot s(\omega) = H_0^1(k(\omega)r) \cdot s(\omega)$. The transfer function is often simply reduced to:

$$\hat{g}(r, \omega) \approx \exp(-jk(\omega)r)/\sqrt{k(\omega)r}. \qquad (2)$$

The use of this acoustic model is widespread in the literature of guided waves, primarily to achieve defect detection and localization purposes [45, 46].

2.2. Space-domain beamforming for plate geometry inference with a single mobile unit

We are considering a mobile platform equipped with an emitter/receiver pair of piezoelectric transducers nearly co-located. At the ith scanning position, the emitter excites the Lamb waves in the plate material with the pulse $s(t)$. Simultaneously, the receiver collects the acoustic response $z_i(t)$ which contains the reflections on the plate boundaries, and it will be assumed that the excitation signal is chosen adequately so that the A0 mode is predominant (while the propagation of S0 is negligible). The objective is to infer the plate geometry and the sensors' acquisition positions in the plate frame. In robotics, this is known as a mapping problem because the displacement between each acquisition position (*i.e* odometry data) is assumed to be known flawlessly. Even though a solution for simultaneous localization and mapping has been proposed [30], the localization problem is disregarded in this paper for the sake of simplicity.

In the considered setup, the acoustic measurements essentially consist of a superposition of the acoustic reflections. Under the assumption that the material is homogeneous, isotropic and the propagation linear, a standard measurement model to reverberation is the image source model [47]. It states that each reflection from the plate boundaries can be considered as a signal originating from a fictional source, deducted from the actual source position and reverberant media geometry. In metal plates, the image source model can be leveraged to account for first order as well as higher-order reflections, resulting in the following measurements in the time domain:

$$z_i(t) = \sum_{\mathbf{x} \in \mathcal{I}(\mathbf{x}_i)} g(|\mathbf{x} - \mathbf{x}_i|, t) * s(t)$$

where $\mathbf{x}_i = [x_i, y_i]$ is the position of the robot during time step i, $\mathcal{I}(\mathbf{x}_i)$ the set of the image sources positions when the real source is in $\mathbf{x}_i$, $g(|\mathbf{x} - \mathbf{x}_i|, t)$ the acoustic transfer function associated to the predominant A0 mode, and $*$ denotes the convolution operation. An example of a clean
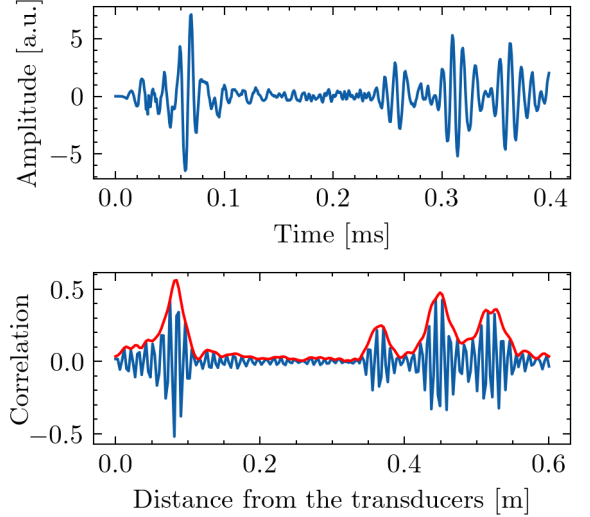

Figure 2: Example of an acoustic signal acquired on an aluminum plate (top plot) and the correlation signal obtained from the measurement along with its envelope (bottom plot). The ranges relative to the first-order reflections (8, 37, 52 cm) can be successfully retrieved from the local maxima. The echo at nearly 45 cm corresponds to a higher-order reflection.

acoustic measurement acquired on an aluminum plate can be seen in Fig. 2, where the transducers have been placed on a 600x450x6mm aluminum plate, and at 8cm of the two edges of a corner.

To retrieve the ranges from the sensors to the plate edges from data $z_i(t)$, we determine the correlation signal:

$$z_i'(r) = \frac{\langle z_i(t), \hat{z}(r, t) \rangle}{\sqrt{\langle z_i(t), z_i(t) \rangle \langle \hat{z}(r, t), \hat{z}(r, t) \rangle}}$$

where $\hat{z}(r, t) = \hat{g}(2r, t) * s(t)$ is the expected signal for the incident wave reflecting at a distance r from the transducers, and $\langle ., . \rangle$ denotes the scalar product in the domain of continuous signals: $\langle u(t), v(t) \rangle = \int_{-\infty}^{+\infty} u(\tau)v(\tau)d\tau$. To alleviate the oscillations present in z_i', we retrieve its envelope $e_i(r)$ with:

$$e_i(r) = |z_i'(r) + j\mathcal{H}(z_i')(r)|$$

where $\mathcal{H}$ denotes the Hilbert transform operator. Thus, the resulting signal e_i yields the distances of the transducers to the metal plate edges with the position of its local maxima. This principle is illustrated in the bottom plot of Fig. 2. Besides, it is noteworthy that a single measurement cannot provide enough information to determine an edge without ambiguity, as all the lines tangent to the circle with radius r and centered at the position of the sensor may equally account for the correlation measurement.

The plate geometry to be recovered is represented by a set of lines: $\mathbf{M} = \{r_l, \theta_l\}_{l=1...4}$ where the parameters (r_l, θ_l) define the line equation in the 2D plane with:

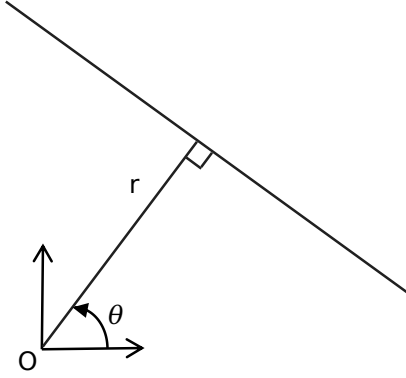$$x \cdot \cos \theta_l + y \cdot \sin \theta_l - r_l = 0$$

4

Figure 3: Representation of lines in a 2-dimensional plane with (r, θ) coordinates.

in a non-mobile frame with respect to the plate, as illustrated in Fig. 3. The origin O of the reference frame can be taken as the initial position of the mobile unit while on the metal panel. Moreover, for convenience, the plate geometry is restricted to rectangular shapes.

Next, given a robot trajectory $\{x_i, y_i\}_{i=1...N}$ (assumed to be flawlessly provided by odometry for the mapping problem), the beamforming map $\mathcal{L}_N$ is computed to assess the likelihood of existence of any line (r, θ) with:

$$\mathcal{L}_N(r, \theta) = \sum_{i=1}^{N} e_i(d_i(r, \theta)) \qquad (3)$$

where $d_i(r, \theta) = |x_i \cdot \cos \theta + y_i \cdot \sin \theta - r|$ is the distance between the robot during measurement step i and the hypothetical line being considered. In the equation, all the correlation values add up constructively along with all the observations if an edge is indeed present. Also, it can be noted that only first-order reflections are taken into account, as we reason on individual lines. One major advantage of this approach is that $\mathcal{L}_N(r, \theta)$ can be computed recursively when an additional measurement e_N is made available, as $\mathcal{L}_N(r, \theta) = \mathcal{L}_{N-1}(r, \theta) + e_N(|x_N \cdot \cos \theta + y_N \cdot \sin \theta - r|)$. This is beneficial for a robotic task meant to be performed in real time, as a map estimate is available at any time, and the computational load of one update is low. Finally, to infer the most plausible plate geometry from $\mathcal{L}_N$, we solve the following optimization problem:

$$\hat{\mathbf{M}} = \arg \max_{\mathbf{M}} \mathcal{L}_N(\mathbf{M}) = \arg \max_{\mathbf{M}} \sum_{l=1}^{4} \mathcal{L}_N(r_l, \theta_l) \qquad (4)$$

where $\mathbf{M}$ is restricted to be a rectangle. It can be solved efficiently by taking that constraint into account. First, one can determine the most plausible line with:

$$(\hat{r}_1, \hat{\theta}_1) = \arg \max_{r, \theta} \mathcal{L}_N(r, \theta).$$

Next, assuming that $\hat{\theta}_1$ provides the most reliable estimation of the plate orientation w.r.t. the robot, the determination of the other lines reduces to solving independent

and straightforward one-dimensional optimization problems:

$$\hat{\theta}_l = \hat{\theta}_1 + \frac{\pi(l-1)}{2} \; ; \quad \hat{r}_l = \arg \max_r \mathcal{L}_N(r, \hat{\theta}_l)$$

for $l = 2, 3, 4$. Solving the plate geometry inference with this approach gives accurate results in laboratory conditions [30]. However, this approach has some limitations. The fact that an infinity of lines can equally account for one reflection causes interference, which is a well-known issue encountered when relying on standard DAS beamforming. The effect of interference is further exacerbated by the high order reflections which are not considered in Eq.(3), whereas their presence cannot be neglected as shown by Fig. 2-b). The consequence is that beamforming maps are fuzzy, which can make the estimation ambiguous, as it will be illustrated later. Also, the method relies on prior knowledge of the propagation model g to obtain accurate results, whereas such a hypothesis may not be realistic for a practical inspection task in challenging outdoor environments, where the structure state is truly unknown.

3. Optimal beamforming for model learning

In this section, we present an adaptive method to recover a metal plate geometry without the assumption of a known model. It is based on focalization in the parameter space (i.e. the propagation model is adjusted) and beamforming for localizing the plate boundaries. First, the parametrization of propagation models using solutions of the Helmholtz equation is presented. Next, we introduce and apply a simple high-pass filter to the beamforming maps to limit the detrimental effect of interference and high-order reflections. A loss function is then designed to assess the focusing capability of a candidate beamformer which should maximize spatial coherency (i.e. the energy that is focused at the geometry estimate on the beamforming map) in the case when the propagation model is appropriate. Finally, an optimizer based on simulated annealing [48] is presented to recover optimal propagation parameters by minimizing the loss in a limited number of iterations. The efficiency of such an approach has been successfully demonstrated for underwater source localization purposes [40, 42].

3.1. Parametrization of the propagation model

With the hypothesis of linear and isotropic propagation, we aim at recovering both a propagation model $\hat{g}(r, t)$ and the plate geometry expressed as a set of lines $\hat{\mathbf{M}} = \{\hat{r}_l, \hat{\theta}_l\}_{l=1..4}$.

For candidate propagation models, we keep relying on the (approximate) solutions of the Helmholtz equation. Hence, estimating the propagation model reduces to the estimation of only three parameters which are the longitudinal velocity c_L, the transverse velocity c_T and the plate thickness d, and that we will gather in the variable

$\Omega = \{c_L, c_T, d\}$. This choice is convenient as we constrain the propagation models to be physically plausible while limiting the search space for the propagation model parameters to a low dimension, which will facilitate the optimization process. As the complete state of the structure may be unknown during the inspection, adapting these wave parameters may be relevant. Indeed, plate thickness may not be known accurately for each surface plate as the structural integrity is unknown. Besides, the effects of variation of temperature, pressure, moisture may be interpreted as variations of the effective velocities. For more complex sources of disturbances such as the effect of coupling or structure irregularities, we are not seeking to strictly compensate for their effect with such a simple model, yet sufficiently enough to predict the plate boundaries location accurately. Next, given candidate values Ω for the model parameters, the dispersion equation for the A0 mode given in Eq. (1) is numerically solved and is used to infer the propagation model $\hat{g}_\Omega(r, t)$ with Eq. (2).

3.2. Design of the loss function

Compared to plate geometry reconstruction with a known propagation model, inferring the plate geometry and propagation parameters simultaneously requires the determination of a larger number of unknowns. Consequently, an appropriate loss function that ideally prevents irregular cost surfaces with many local minima is needed to facilitate the optimization process.

Here, we introduce a loss function to assess the ability of a candidate beamformer (related to candidate parameter values Ω) to focus the energy of the wave packets contained in the measurements at the plate geometry estimate so that minimizing the loss function w.r.t. the model parameter search space improves the spatial coherency achieved with the beamformer. For candidate propagation parameters, the beamforming map $\mathcal{L}_\Omega(r, \theta)$ is constructed as in Eq. (3), allowing a plate geometry estimate $\hat{\mathbf{M}}_\Omega$ to be retrieved from it with the same optimization process as in Eq. (4). We then evaluate the total energy focused at the estimate $\hat{\mathbf{M}}_\Omega$ over the beamforming map that has been high-pass filtered to limit the effect of interference and high-order reflections. The filtered map value at each line (r, θ) is simply defined by the difference between its initial energy value and the minimum of energy in its vicinity that is to be appropriately defined:

$$\tilde{\mathcal{L}}_\Omega(r, \theta) = \mathcal{L}_\Omega(r, \theta) - \min_{(r', \theta') \in V(r, \theta)} \mathcal{L}_\Omega(r', \theta'). \quad (5)$$

where $V(r, \theta)$ refers to the set of lines in the vicinity of (r, θ). Compared to the standard $\mathcal{L}_\Omega(r, \theta)$, the filtered map $\tilde{\mathcal{L}}_\Omega$, while being inexpensive to compute, has the advantage to present fewer areas where the intensity is high but homogeneous (such a situation occurs due to the combination of high-order reflections and interference). Hence, it is more compatible with Eq.(4) for the determination of the location of the edges. Thus, using Eq. (5) may appropriately filter "fuzzy" areas where the energy is spread

homogeneously (*i.e.* not focused at a single point) due to interference on the beamforming maps, and may isolate correct intensity peaks. This will be illustrated next with experimental data.

To simultaneously recover propagation parameters and the plate geometry, performing a joint search in both the propagation model space and the geometry space would be computationally expansive. Instead, we rely on an optimal beamforming formulation: the loss is only evaluated over candidate model parameters Ω, and for the corresponding geometry estimate $\hat{\mathbf{M}}_\Omega$ retrieved *from the high-pass filtered beamforming map* $\tilde{\mathcal{L}}_\Omega$ with Eq.(4). The loss value $l(\Omega)$ that we will seek to minimize is then taken as minus the sum of the intensity levels evaluated at the retrieved edges:

$$l(\Omega) = - \sum_{(r, \theta) \in \hat{\mathbf{M}}_\Omega} \tilde{\mathcal{L}}_\Omega(r, \theta) \quad (6)$$

so that the energy focused at the plate geometry estimate can be maximized, while the detrimental effects of interference and high-order reflections can be minimized. The geometry estimate provided by the optimal beamformer is expected to match closely the ground truth geometry due to the maximum of spatial coherency as long as measurements have been acquired on a sufficient portion of the plate surface. Besides, to highlight the benefit of using high-pass filtered beamforming maps, propagation model selection based on the loss evaluated using the regular beamforming map $\mathcal{L}_\Omega(r, \theta)$ will also be carried out in the following sections, and the mapping results will be compared.

3.3. Optimization with simulated annealing

An optimization process is needed to adjust the wave propagation parameters (longitudinal and transverse velocities and the plate thickness) through the minimization of the loss function. Due to the implicit definition of the propagation models, first-order methods such as gradient descent are impractical to use for our problem.

Simulated annealing [48] is efficient for estimating a global minimum of a cost function, even when the number of unknowns is large [42]. This metaheuristic is inspired from metallurgy where, to form a perfect crystal (which corresponds to the state of minimal energy), a pure liquid substance is slowly cooled. At each iteration of the optimization process, a random perturbation is applied to the current point value. The perturbation is systematically accepted if the energy is decreased. To escape local minima, the perturbation is accepted according to a Boltzmann probability distribution if the energy is increased. The temperature, which is a hyperparameter, is decreased slightly after each iteration so that the probability to increase the energy goes to zero. Hence, the major controllable parameters of simulated annealing are the distribution of the perturbation and the profile of the temperature cooling.

For Lamb-wave based mapping without a prior propagation model, the parameter search is reduced to the optimization over the value of Ω as the geometry is directly deduced using Eq. (4) when Ω is fixed. Our implementation of the optimizer is similar to that used in articles related to the underwater localization problem [40]. The major difference lies in the cost function design. First, we initialize the propagation parameters with uniform distributions within predefined intervals which are plausible regarding the application:

$$c_L^0 \sim \mathcal{U}([c_{\min}, c_{\max}]); \quad c_T^0 \sim \mathcal{U}([c_{\min}, c_L^0 - m])$$
$$d^0 \sim \mathcal{U}([d_{\min}, d_{\max}]).$$

The value of c_T is drawn below the value of c_L, with a small margin $m > 0$, as it cannot physically be higher (*i.e* there are no positive real-valued solutions to the Rayleigh-Lamb equation).

At each iteration of the algorithm, the parameters are randomly disturbed using the following perturbations:

$$c_L^{t+1} = \min\left\{\max\{c_L^t + \Delta c \cdot \chi_0^3, c_{\min}\}, c_{\max}\right\}$$
$$c_T^{t+1} = \min\left\{\max\{c_T^t + \Delta c \cdot \chi_1^3, c_{\min}\}, c_L^{t+1} - m\right\}$$
$$d^{t+1} = \min\left\{\max\{d^t + \Delta d \cdot \chi_2^3, d_{\min}\}, d_{\max}\right\}.$$

Using the min-max formulation enables to leverage prior information by constraining the parameter values within plausible intervals. Similarly to the initialization step, c_T^{t+1} is restricted to be lower than c_L^{t+1} with the same margin m. χ_0, χ_1, χ_2 are independent random values between -1 and 1, and are drawn from uniform distributions: $\chi_{1,2,3} \sim \mathcal{U}([-1,1])$. They are raised to power 3 so that small variations are more likely. Still, large variations can be possible to explore regions of the search space that are far occasionally when the values of Δc and Δd are chosen to be large enough.

Next, for the new parameter values Ω^{t+1}, the dispersion relation $k_{\Omega^{t+1}}(\omega)$ is determined by solving the Raleigh-Lamb equations. As the relation is computed numerically at each iteration of the optimization process, the computational load can be quite demanding. A trick to save computational time is to determine the wavenumber only for a restricted set of pulsation values $\omega_1, ..., \omega_K$ and to use linear interpolation to determine the wavenumber for other frequencies.

Next, the acoustic transfer function $\hat{g}_{\Omega^{t+1}}(r, \omega)$ is determined with the Helmholtz model given in Eq. (2). The beamforming map $\mathcal{L}_{\Omega^{t+1}}(r, \theta)$ is then computed and a plate geometry estimate $\hat{\mathbf{M}}_{\Omega^{t+1}}$ is retrieved from it, allowing the determination of the loss value $l(\Omega^{t+1})$ with Eq. (6).

The variation of energy between the previous and disturbed parameters is $\Delta E = l(\Omega^{t+1}) - l(\Omega^t)$. In the context of simulated annealing, the disturbed parameter value is not systematically kept. It is the case only when:
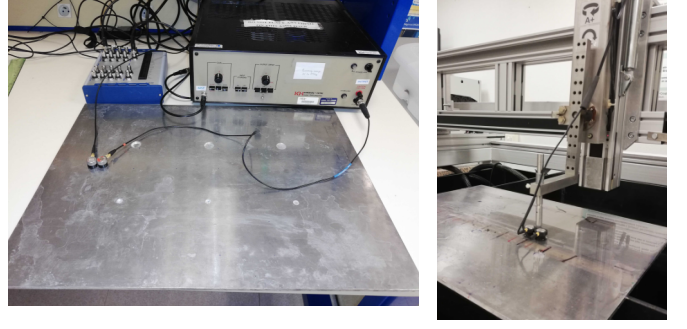
$$\chi < \exp\left\{-\frac{\Delta E}{\gamma T}\right\}$$

Figure 4: Pictures showing the experimental setups for Scenario 1 (left) and Scenario 3 (right).

where γ is a strictly positive scaling parameter, T is the temperature at the iteration t, and χ is drawn randomly and uniformly between 0 and 1. Consequently, when the energy is decreased, the disturbed parameters are systematically kept. Otherwise, the acceptance rate is given by the Boltzmann distribution which yields lower acceptance rates for more significant increases of energy. The temperature parameter is often chosen to decrease inverse logarithmically. To enable fast convergence of simulated annealing, we will decrease the temperature inverse linearly. Trials and errors are used to determine appropriate parameters for the optimizer: the values that empirically demonstrate a lower likelihood for the optimizer to be stuck in local maxima while maintaining a sufficient convergence speed are retained.

As it has already been highlighted, the cost function may be heavy to assess, in particular when the number of considered measurements is high. Indeed, each iteration of the optimizer requires solving the Rayleigh-Lamb equation for a set of frequency values, then computing the beamforming map using the N measurements, and recovering a plate geometry estimate with the optimization. For a robotic application, a few seconds might be needed to achieve convergence with around 100 measurements and using a linear decrease of the temperature. Thus, our method cannot be used in real time. Yet, this is not an issue, as it could be considered, during a practical robotic inspection task, to stop the robot for a few seconds to run the optimizer occasionally, and restrict the maximum number of acoustic measurements used to perform the optimization.

4. Experimental setup

We test our approach on experimental acoustic data that have been acquired in three different scenarios. To generate the datasets, an emitter/receiver pair of contact piezoelectric V103-RM U8403008 transducers is moved at different positions on the plate surface, in each scenario. These transducers are used because, at the time of the experiment, it was the best solution available to the authors to generate and receive Lamb waves, although it may not be optimal. During the acquisition, the transducers
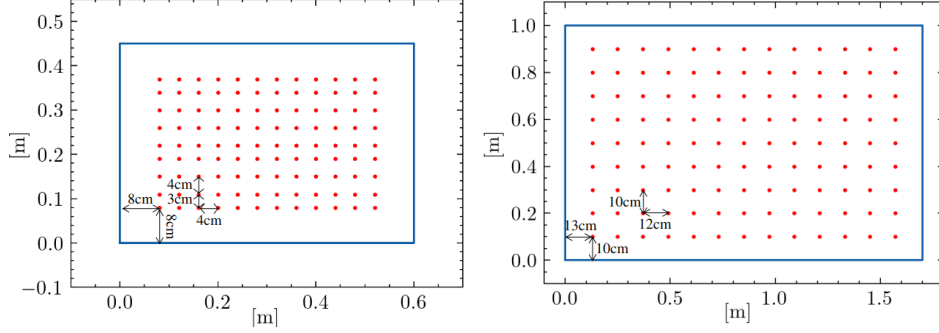
Figure 5: Acquisition positions on the aluminum plate for Scenarios 1 and 3 (left), and on the steel plate (right).

are placed one beside the other to approximate a pulse-echo setup. The excitation signal used to emit the waves in the material corresponds to two tone bursts of a sinusoidal wave at 100 kHz, with an amplitude of 100 Volts peak to peak. This frequency is chosen as it has been experimentally observed that the predominant propagation mode was A0 for all the scenarios, and the others modes are almost nonexistent. It is to be noted that, in our experiments, two different transducers are used, whereas our method is based on a point-like and co-located emitter-receiver assumption that we assimilate to the center between the transducers. This is not a significant problem as the diameter of the transducers (1.7cm), and thus the distance between their centers is not large compared to the wavelength (2 cm) for the considered excitation frequency. Thus, the difference induced by this setup has negligible impact on the signals.

Different operations are performed next on the measurements. For Scenario 1 and 2 only, 10 scans are acquired per acquisition position and are averaged to improve the signal-to-noise ratio. This operation is performed although it is not critical in a laboratory environment. In addition, the high frequencies (> 400 kHz) of the signals are filtered out. Also, the equivalent of twice the excitation duration is smoothly removed at the beginning of each measurement with a sigmoid window. Indeed, it is not desirable to keep the first wave packet resulting from the direct transmission of the excitation between the emitter and the receiver, as it does not correspond to a reflection on a plate boundary. The counterpart is that transducers cannot be brought closer to an edge than the dead-zone distance (which amounts here to 2 to 4 wavelengths), otherwise, the first reflection on it would be removed as well.

For Scenario 1, the transducers are moved by hand manually on an aluminum plate of size 600x450x6 mm that contains artificial holes of different thicknesses and depths as shown in Fig.4-a). In total, $N_1 = 108$ measurements are acquired, each of them containing $M_1 = 500$ samples collected at a sampling rate of 1.25 MHz. The signals are acquired with a National Instruments USB 6356 data acquisition device. For Scenario 2, the data is collected with an oscilloscope on a steel plate of dimensions 1700x1000x6 mm. With these data, we can test our approach on a different material and show that it is still applicable to a larger surface. A total of $N_2 = 117$ measurements are collected with a sampling frequency of 6 MHz. The total number of samples per measurement is $M_2 = 5000$. For Scenarios 1 and 2, the transducers are in contact with the surface during the acquisition. Coupling gel is placed at their interface to ensure a good coupling. For Scenario 3, the data are acquired on the same plate as the one used for Scenario 1. However, a thin layer of water of approximately 1 mm of thickness is put all over the plate surface, and the transducers are not placed in contact with the plate surface during the acquisition, but are kept in contact with the water only. The acquisitions are performed using a customer-design five axes immersion scanner made by Inspection Technology Europe BV. It is also used to place the transducers (that are kept one beside the other) at specific positions on the measurement grid while maintaining a constant distance between the plate surface and the transducers. Due to the plastic holder, the distance between the centers of the transducers rises to 2.5cm which is not an issue, as the distance is not large comparing to the wavelength. For this scenario, a total of $N_3 = 108$ measurements are collected at the same positions than those used for Scenario 1, the sampling frequency is 1.25 MHz, and the number of samples per measurement is $M_3 = 500$. The data acquired in this setup are expected to be representative of those that would be acquired on a real structure by the robotic system, where water may also be used as coupling, and where the transducers may not be directly in contact with the structure surface to avoid damaging them by surface irregularities. Furthermore, this scenario will also allow us to highlight the potential of our approach in a slightly "disturbed scenario" comparing to the nominal acquisition conditions of Scenarios 1 and 2. Pictures of the experimental setups are available in Fig. 4, and all the acquisition positions are provided in Fig.5.

In the next, we do not assume any imprecision on the sensor displacements. Indeed, Simultaneous Localization and Mapping has been studied elsewhere [28, 30], and the method presented here is expected to integrate these frameworks conveniently.
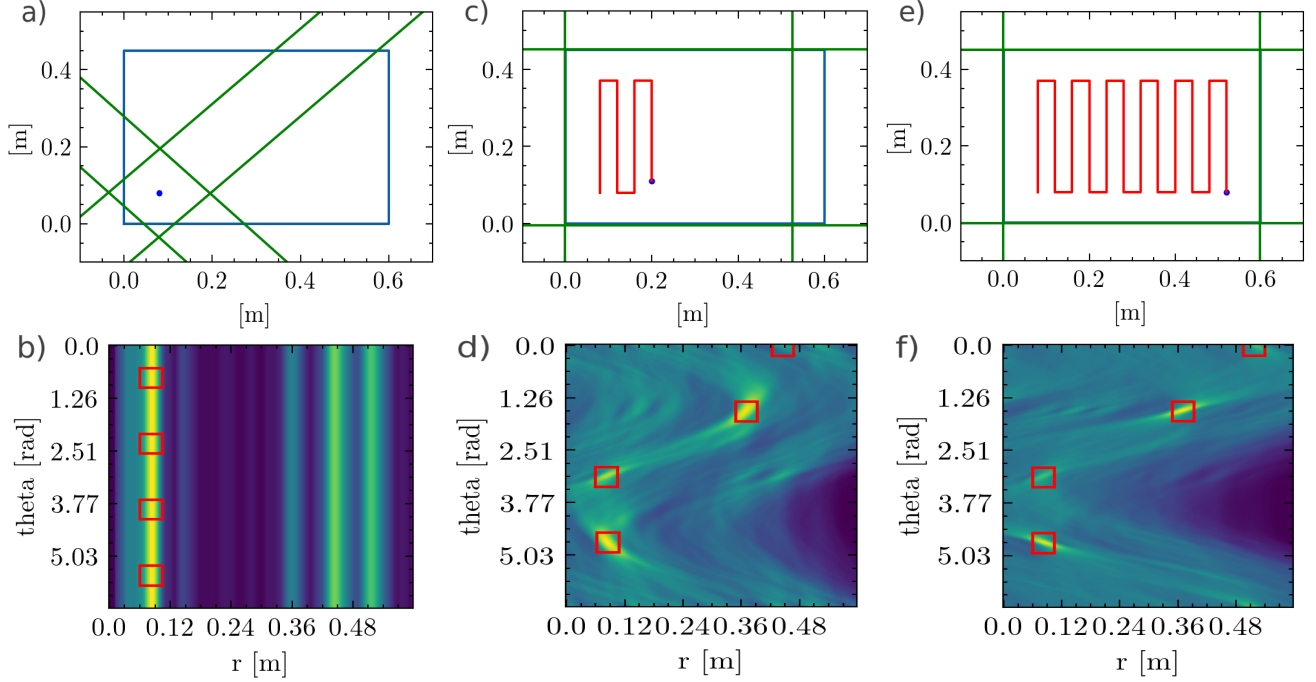
8

Figure 6: Mapping results based on the standard DAS beamforming with a predetermined propagation model at different steps of a simulated lawn-mower trajectory in Scenario 1. Measurements steps 1, 35 and 108 correspond to figures a), c) and e) respectively where the geometry estimate is represented by the straight lines. The corresponding beamforming maps are given in figures b), d) and f) along with the retrieved edges indicated by the rectangles.

5. Results

This section illustrates the efficiency of our approach for mapping a rectangular metal panel using ultrasonic guided waves in the three aforementioned scenarios. The benefit of filtering the beamforming maps is first discussed and highlighted based on the experimental data. Next, the correlation between the designed loss function and the reconstruction error is numerically assessed. The optimizer designed in the previous section is run to simultaneously infer the plate geometry and recover the propagation model. The resulting precision is compared with that obtained using a predetermined propagation model that will be used as a baseline. The overall results demonstrate that this target objective is successfully achieved with our method in nominal acquisition conditions (Scenarios 1 and 2). Our approach is also tested in slightly disturbed conditions (Scenario 3) to illustrate that it remains efficient. The results are obtained using the full batch of measurements in each scenario, which would amount to having the robot covering an important portion of the plate surface before calibrating the propagation model. As this may not be a representative scenario, the efficiency of our procedure is also assessed with simulated robot paths with acquisition points that are more sparse, and with a varying number of measurements available during the calibration.

5.1. Mapping with a predetermined propagation model

In Fig. 6, we show the mapping results for a lawn-mower trajectory simulated with the data from Scenario 1, and during measurement steps 1, 35 and 108. The geometry estimates are determined at each measurement step from the standard beamforming maps derived with Eq. (3), and based on a predetermined propagation model which is built using Eq.2 and predetermined model parameters ($d = 6$ mm, $c_L = 6420$ m/s and $c_T = 3040$ m/s for our aluminium plate which were validated by comparing the theoretical and experimental dispersion curves). It can be observed that, initially, only the range to the closest edge is retrieved, but the orientation estimate is essentially random as only a single measurement has been integrated. During Step 35, three plate edges are correctly recovered but it is not the case of the right boundary as it is further away. Eventually, the geometry is fully recovered during Step 108, when all the available measurements have been integrated. The final average reconstruction error is less than one degree for the orientation, and the average estimation error is 0.15cm for the lines range parameters. Overall, these results illustrate the efficiency of space-domain delay and sum beamforming combined with our grid search method for mapping the plate geometry with a propagation model based on prior knowledge of the mechanical properties of the material. This method is efficient despite the artificial holes that are present in the plate.

We now perform the experiment using all the measurements acquired on the larger steel plate (Scenario 2). This time, the parameters for the propagation model are $d = 6$ mm, $c_L = 5880$ m/s and $c_T = 3250$ m/s. The beamforming map shown in Fig. 7-a) depicts two visible intensity peaks. The two other peaks are much less visible due to
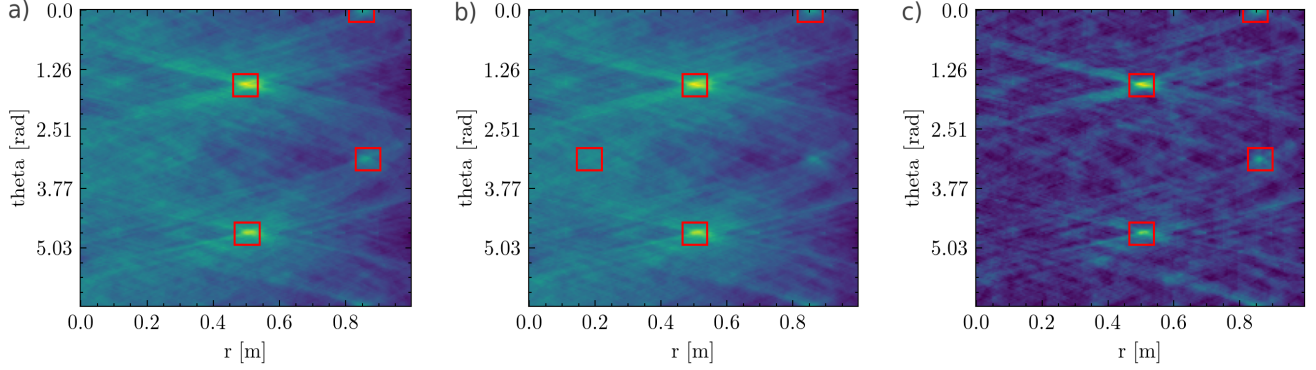
9

Figure 7: Different beamforming maps computed using the data from Scenario 2 and the retrieved edges. a) shows the standard beamforming map, which yields correct estimates. b) depicts the map obtained with the same data sub-sampled in time. One edge is not correctly estimated. c) shows the high-pass filtered beamforming map obtained from the sub-sampled data. The correct plate geometry is recovered, while the fuzzy areas due to interference and higher-order reflections have been partially filtered out.

their lower intensity, and can be easily mistaken with interference and high-order reflections which cause areas of homogeneous intensity. Although the estimation is correct in this case (the average range error for the line estimation is approximately 0.5 cm), it may not be robust. To illustrate this, we sub-sample in time the data by a rate of 4 and reconstruct the beamforming map using the same propagation model. The results can be seen in Fig. 7-b). The beamforming map is very similar. However, all but one line are still correctly recovered, causing the average error on the estimation of the line ranges to rise to 17cm as the ambiguity is too important. Using high-pass filtered beamforming maps may increase the robustness of the estimate as described earlier. Such a map is shown Fig. 7-c) where $V(r, \theta)$ is chosen as the rectangular area centered at (r, θ) with a size 6.5cm × 24°. This window is sufficiently large to encompass the intensity peaks on the beamforming map, and sufficiently limited to make the filtering effective. When relying on the filtered version of the beamforming map, the estimation is made correct (the range error is again 0.5cm), even though we cannot completely alleviate the effect of interference and higher-order reflections. Hence, the filtering may provide additional robustness which is to be leveraged to calibrate the propagation model. It may be even more useful in the presence of disturbances during the acquisition, as will be illustrated in the following.

5.2. Correlation between the loss and the geometry estimation error

We assess whether the designed loss is sufficiently correlated with the reconstruction error to ensure that its minimization yields an accurate plate geometry estimation. We create a family of 40 propagation models based on the approximate solutions to the Helmholtz equation Eq. (2) with values of $\Omega = \{c_T, c_L, d\}$ uniformly distributed within the intervals $c_T, c_L \in [2500\text{m/s}, 6500\text{m/s}]$ and $d \in [3\text{mm}, 7\text{mm}]$. Then, we determine the filtered beamforming map using each model to obtain a plate ge-

ometry estimate in each of the three scenarios under consideration. The results are displayed in Fig. 8 as plots of the reconstruction error (both in range and orientation) w.r.t. the loss value. We also display the same plots using the geometry estimates and loss values obtained without the filtering, for comparison. Ideally, we would obtain reconstruction errors that would monotonically decrease with the loss value.

For both Scenarios 1 and 2 in Fig. 8-a)-d), we observe that the range errors globally diminish for lower loss values. It can also be observed that models with close loss values can yield completely different reconstruction errors, or that models with high loss values can provide an accurate estimate (*e.g* the plot of the range error in Fig. 8-c)). Yet, these tendencies are not critical, as the major requirement for our approach to be effective is that the best estimation results are achieved for the lower losses as this is what will be minimized. The variations of the orientation error present a different aspect. There is no strict decrease in the error for lower losses. Also, the discretization of the orientation value is visible due to the resolution of the beamforming map that is limited for the sake of computational efficiency. Yet, it is still possible to achieve an accuracy in the order of one degree, which is sufficient for our application. Also, the limited resolution is not a significant problem for propagation model learning, as the best accuracies are also achieved for the lower loss values.

We notice a slightly more divergent behavior for the two losses in Scenario 3, which corresponds to our slightly disturbed scenario. Regarding Fig. 8-f) where the beamforming maps are not filtered, the reconstruction error presents a tendency to decrease for lower loss values. However, the minimum reconstruction error is achieved for a loss value of approximately $l(\Omega_{\min}) = -86$, and it becomes higher for lower losses. This is not the desired behavior, as it would result in poorer estimation results if the loss minimization is effective. This tendency is not visible when the loss values and the geometry estimates are obtained from
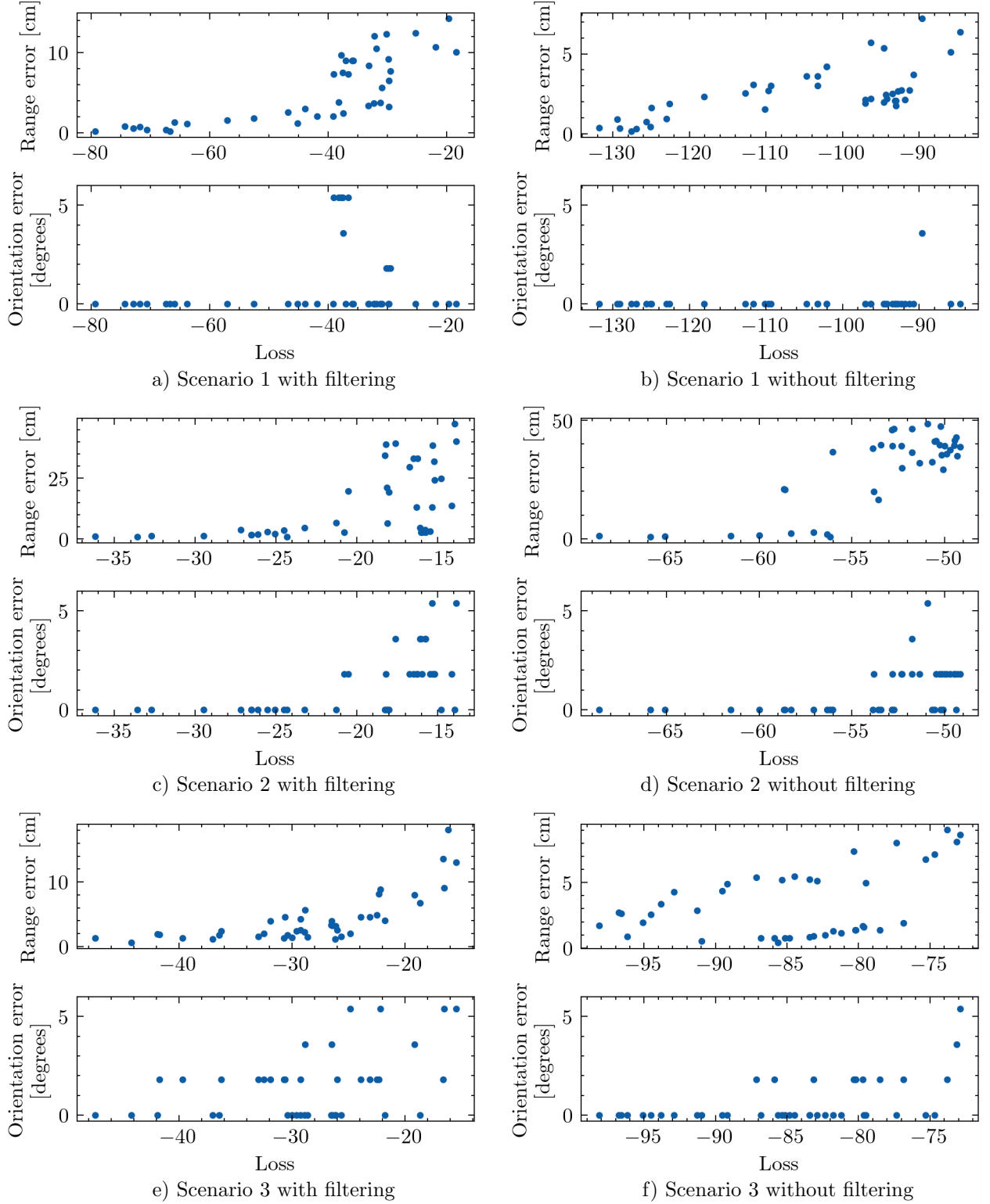
10

Figure 8: 2D plots showing the correlation and loss values achieved using each of the propagation models from the predefined model set, and for the three scenarios. On the left, the loss value and geometry estimates are determined from the high-pass filtered beamforming maps. On the right, they are determined from the standard maps without filtering.
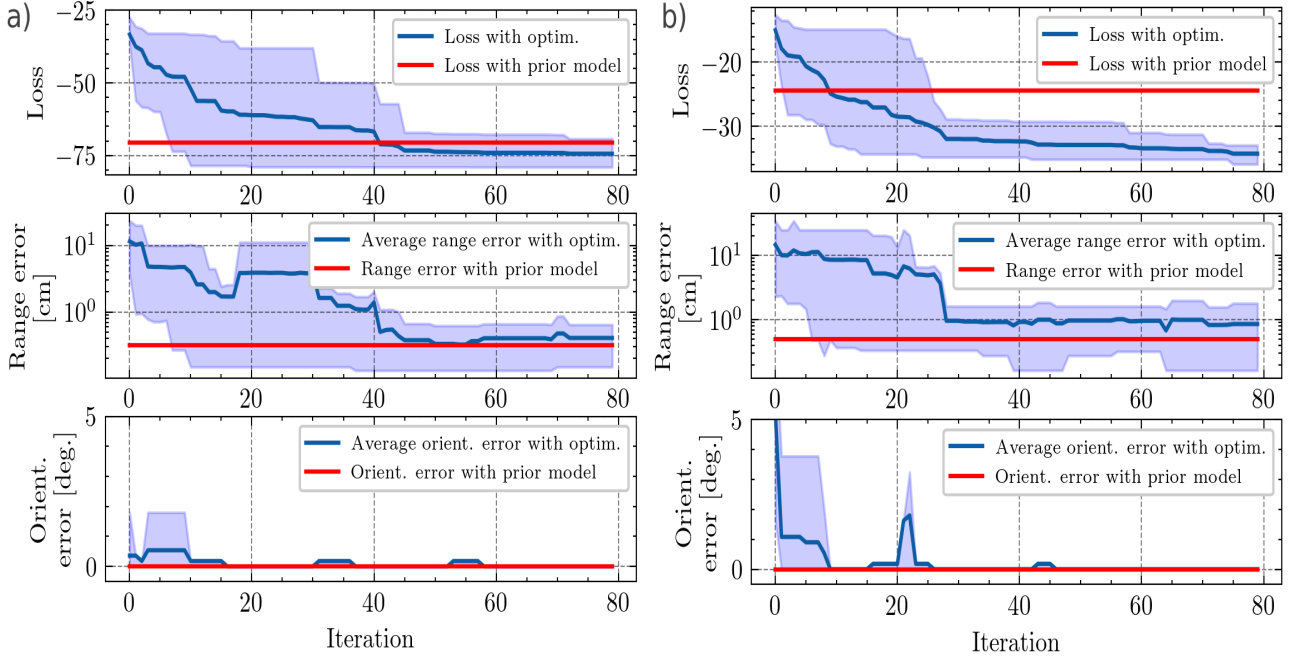
Figure 9: Evolution of the loss value and reconstruction errors for 10 repetitions of the optimization process with simulated annealing, and using the data from Scenario 1 (a) and Scenario 2 (b). The solid lines represent the mean values. The upper and lower bounds of the filled areas represent the minimum and maximum values respectively during each iteration. For comparison, the values achieved with the predetermined propagation model for each scenario are displayed as horizontal lines. The scale along the y-axis is logarithmic for the range error plots only.

the high-pass filtered beamforming maps (Fig. 8-e), where the lowest reconstruction errors are globally obtained for the lower losses. Hence, these results support the benefit of high-pass filtering the DAS beamforming maps for mapping and propagation model adaptation. It provides additional robustness due to its ability to lower the detrimental effect of high-order reflection and interference.

5.3. Model learning and plate mapping in nominal acquisition conditions

To assess the performance of our approach for optimal beamforming for Lamb wave-based mapping, we run it 10 times for Scenario 1 and 2, with random initial parameter values for each repetition. The simulated annealing is set with the following parameters: $\Delta c = 7000 \text{m/s}, \Delta d = 2\text{cm}, c_{\min} = 1500\text{m/s}, c_{\max} = 8000\text{m/s}, m = 500\text{m/s}, \gamma = 1, T = T_0/t$ where $T_0 = 200, d_{\min} = 3\text{mm}$ and $d_{\max} = 1\text{cm}$. Besides, the performance of our approach is compared with the results achieved when using predetermined propagation models based on prior knowledge of the plate thickness, the longitudinal and transversal velocities in nominal conditions. These predetermined models will serve as a baseline for comparison. Fig. 9 depicts the evolution of the minimum loss value and the corresponding reconstruction errors achieved during the optimization process. The upper and lower bounds of the filled areas represent the minimum and maximum values over the 10 runs, at each iteration step, while the solid blue lines account for the mean values. For comparison, the loss values

and reconstruction errors achieved when using the predetermined propagation models for the two scenarios are also displayed.

In both scenarios, the achieved minimum loss decreases monotonically until it reaches a plateau. The final loss value is always lower than the loss value achieved with the predetermined model in Scenario 1 and significantly lower in Scenario 2. In terms of reconstruction error, the final average range error is comparable to that achieved with the predetermined model, which is 3mm for Scenario 1. It is slightly above the estimation error value obtained with the predetermined model (0.5cm) for Scenario 2. Besides, the orientation errors rapidly decrease to zero for all the runs, achieving the same precision as the predetermined models in the two scenarios.

Altogether, these experiments demonstrate that a propagation model can be efficiently recovered to estimate a plate geometry through optimal beamforming by relying directly on data, regardless of the plate size and material, and as long as the measurements have been acquired on a sufficient portion of the surface.

5.4. Model learning and plate mapping in non-nominal acquisition conditions

We perform the same experiments using the data from Scenario 3 which have been acquired in slightly disturbed conditions due to the layer of water that is placed at the interface between the transducers and the plate surface. The evolution of the loss and the reconstruction errors for 10
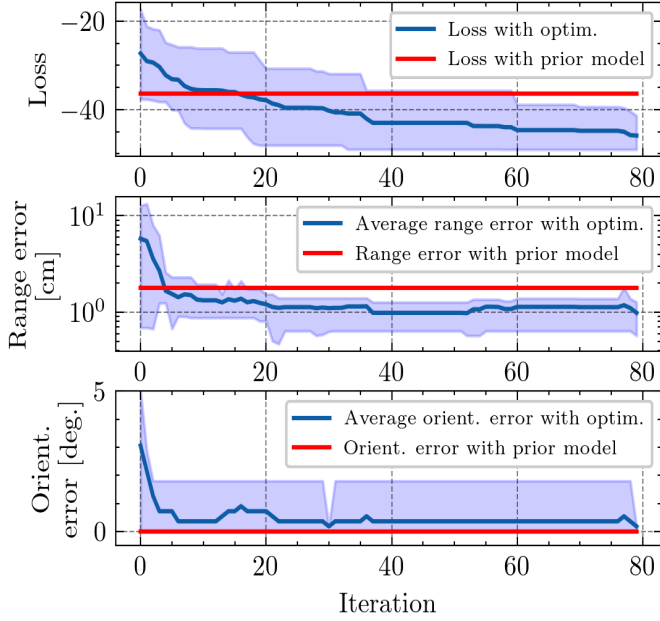
12

Figure 10: Evolution of the loss value and reconstruction errors for 10 repetitions of the optimization process and using the data from Scenario 3. The blue lines represent the mean values. The upper and lower bounds of the colored areas represent the minimum and maximum values respectively during each iteration. For comparison, the values achieved with the predetermined propagation model are displayed as horizontal red lines. The scale along the y-axis is logarithmic for the range error plot only.

repetitions of the optimization process with random initial parameter values are shown in Fig. 10. It can be observed that the loss rapidly decreases to a value lower than that achieved with the predetermined model. Regarding the reconstruction error, the average range error, after convergence, reaches 1cm while the error is 2cm when using the predetermined model for the geometry reconstruction. Furthermore, the orientation error rapidly decreases to a value lower than one degree.

Altogether, our approach, which automatically calibrates the propagation model based on data, yields better geometry estimates in this disturbed scenario compared to mapping with the predetermined propagation model, as illustrated by Fig. 10. These results are promising as the propagation in the thin layer of water has not been modeled explicitly. This further shows the potential of our approach which adapts the propagation model to achieve accurate plate reconstruction in varying conditions, as it is expected to happen for a robotic inspection task on large structures in challenging outdoor environments. Also, with our approach, there is potentially no need to take into account slight sources of disturbance explicitly in the propagation models.

5.5. Non uniqueness of the optimal model parameters

Although we have shown that a propagation model can be recovered based on data to achieve precise localization by adapting the model parameters, our method cannot

recover the real values of the physical model parameters. Indeed, different model parameters can yield equivalent loss values as depicted by Fig. 11, where we represent the variation of the loss w.r.t. the two velocity parameters for a fixed thickness (d = 6mm), and using the data acquired on the two metal plates considered in this study (Scenario 1 and 2). The more specific explanation is that different model parameters may lead to similar dispersion values in the considered frequency bandwidth, after resolving the Rayleigh-Lamb equations. Yet, the fact that the actual model parameters cannot be recovered with our method is not a significant issue, as our primary objective is to achieve accurate mapping of the plate structure with a calibrated model g, so that the wavepackets inside the measurements can be appropriately accounted for.

5.6. Evaluation of our approach with sparse measurements

During a real robotic inspection task, the acoustic measurements may not have been acquired over a dense grid, and over a sufficient portion of the surface during the calibration operation to fully recover the plate geometry. To evaluate the performance of our approach in more realistic scenarios, we assess how the quantity of measurements available during the optimization process affects the propagation model selection when the data are acquired along more realistic trajectories. To avoid running the optimizer every time, we consider the previous family of 40 propagation models. We evaluate, for each propagation model, the reconstruction errors obtained with and without filtering the beamforming maps, and select the error relative to the propagation model, for every set of measurements, that yields the lowest loss value. We also assess the estimation errors when the predetermined propagation model is used along with high-pass filtered beamforming maps, for comparison. We design two different trajectories (one for each plate) that are provided in Fig.12. The results, which are shown in Fig. 13, were obtained using the data acquired on the large steel plate (Scenario 2) and using the data acquired in the disturbed conditions (Scenario 3).

When only a few measurements are available, the average range errors are relatively high in all the cases, because the sensors need to pass by a border closely enough to detect it. The most accurate results are achieved when all the measurements are taken into account. In the middle, we can see, in Fig. 13-a), that the minimum range error is reached faster when the beamforming maps have been filtered, and this minimum error is lower than the error achieved with the predetermined model. Furthermore, both in Fig. 13-a) and b), the reconstruction errors are seemingly lower when relying on model calibration for the reconstruction. Overall, the results show that our approach is effective for mapping, and yields similar - if not better - performance than that obtained with a predetermined propagation model, even when the measurements have been sparsely acquired by the mobile unit.
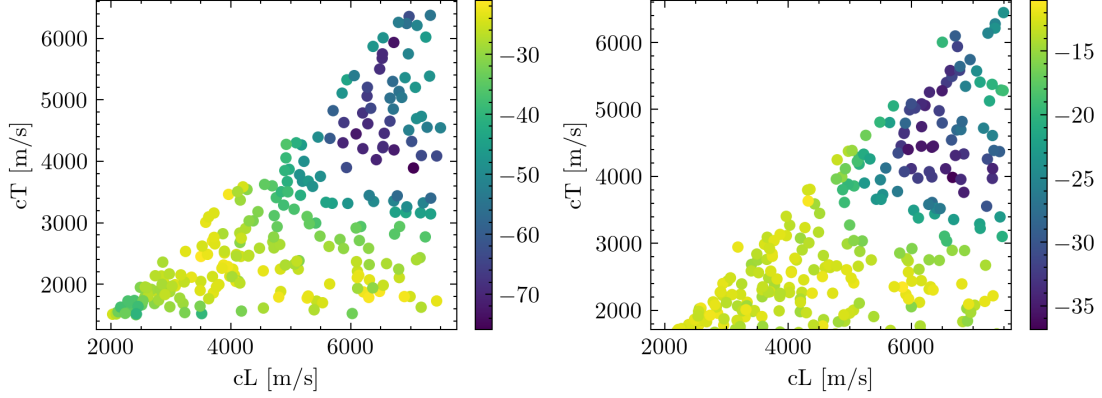
Figure 11: Loss value computed on the high-pass filtered beamforming maps with respect to the longitudinal and transverse velocities. The data from Scenario 1 are used for the plot on the left, while the data from Scenario 2 are used for the plot on the right.
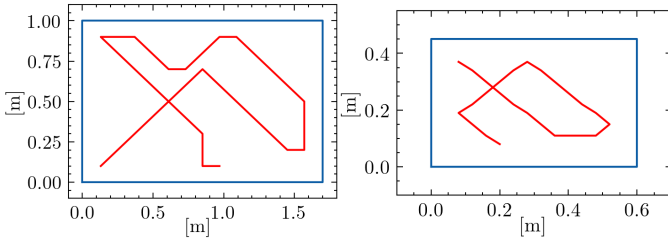

Figure 12: Simulated robot paths used for the experiments on the steel plate (left) and the aluminum plate (right). The path lengths (*i.e* the number of acquisition positions) are respectively 36 and 26.

6. Discussions

The method presented here restricts the propagation models to be approximate solutions of the Helmholtz equation with dispersion relations derived from the Rayleigh-Lamb equation. This approach is not sufficient for recovering the actual model parameters, and addressing this in future work would be desirable for a complete NDT method (the knowledge of plate thickness variation would be of particular importance). Yet, the recovered propagation model $\hat{g}$ is sufficient to achieve accurate mapping results through beamforming. Whether this approach remains appropriate in more realistic conditions (*i.e* on a real ship hull for example) is still subject to investigation. It is expected that this parametrization would be sufficient as long as the first-order wave-packets are sufficiently energetic within the measurements, and that the major hypotheses on the propagation model (linear propagation, homogeneous and isotropic material) approximately hold. Due to the large size of the plates on a real structure and the low reflectivity of weld joints, the signal-to-noise ratio (SNR) is expected to be low. Hence, a study evaluating the performance of our approach for various SNR conditions is needed to assess how likely it would work in practice. Also, it is to be noted that, in the present study, the sensor positions were measured accurately, whereas in practice, only estimated positions will be available.

The case of multi-modal propagation is not considered here, whereas it is likely if the frequency is not sufficiently adequate to the material in a -presumably- unknown state, or if mode conversion occurs. Having at least A0 and S0 modes propagating simultaneously is the most frequent scenario. It is believed that the algorithm could be extended by considering several hypotheses (bi-modal, A0-only, S0-only propagation, mode conversion for different paths, see [4]) to determine which one is most likely based on data. However, integrating more complex interactions such as diffraction due, for example, to complex structural features such as stiffeners, holes... would be more challenging. We expect isotropic propagation to be prevalent, as these complex wave interactions may be scarce and have a sufficiently small incidence on the signals to not affect the mapping results.

Besides, our method, as presented here, is restricted to rectangular geometries, as it facilitates edge retrieval from the beamforming map. This constraint is not a limitation for mapping storage tanks or ship hulls, as they are almost entirely made of rectangular panels. Yet, our approach could be extended in future work to make it applicable to structures with more general geometries. One may also want to adapt our approach to more conventional applications in SHM where, for example, the propagation model could be automatically calibrated by maximizing the energy focused at the estimated defect location on the imaging results, or by relying on the reflections on the sample boundaries.

7. Conclusion

In this paper, we introduce a method to accurately recover the geometry of a metal plate by relying on ultrasonic measurements acquired by a mobile unit, in pulse-echo, and without using a predetermined propagation model. Our approach is based on focalization in the model parameter space and beamforming for localization of the plate boundaries. We restrict the propagation model to be an approximate solution of the Helmholtz equation and parameterize it with only three physical values. We introduce
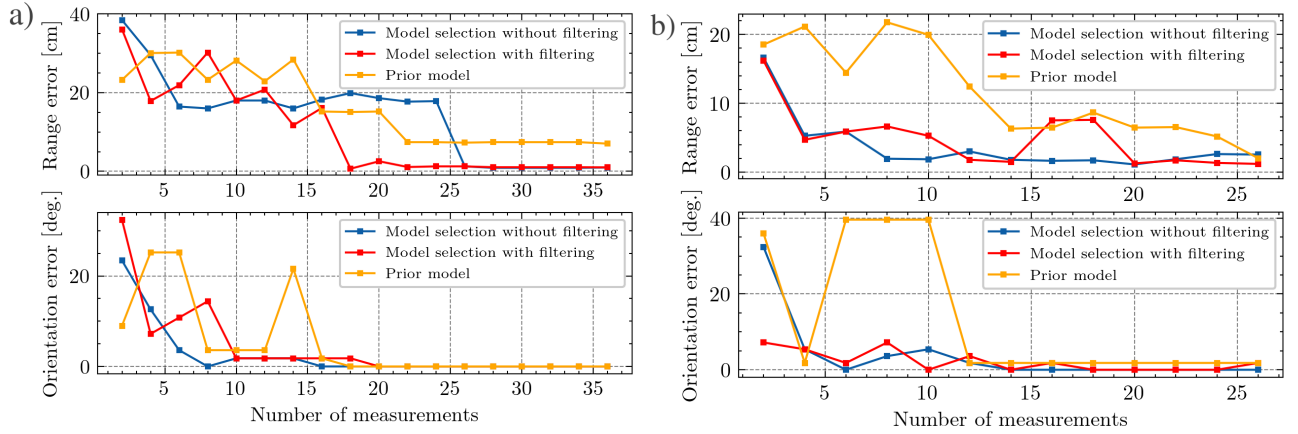
14

Figure 13: Reconstruction errors w.r.t. the number of measurements considered in the loss, and using the data from Scenario 2 (a) or from Scenario 3 (b). The measurements are integrated one after the other in the loss, following the simulated paths. The error is only evaluated for the model yielding the lower loss value for the two cases (model selection with and without filtering the beamforming maps). For comparison, the errors achieved with the predetermined models are also displayed.

a loss function assessed on high-pass filtered beamforming maps to quantify the focusing ability of a candidate beamformer (*i.e.*, candidate model parameters). Eventually, we find optimal model parameters with a simulated annealing optimization process.

We demonstrate the performance of our method on three sets of experimental acoustic data acquired on a dense grid on two metal plates of different sizes and different materials. The results illustrate the relevance of filtering the beamforming maps to reduce the impact of interference and high-order reflections. We also show that a propagation model enabling accurate boundary localization can be recovered with simulated annealing. For the two undisturbed scenarios, the precision of the localization is found to be similar to that achieved with the model built from prior knowledge on the plate material, but it is found to be superior in non-nominal acquisition conditions. This highlights the very potential of our method for Lamb wave-based localization and mapping on a large metal structure, where the wave propagation conditions may not be known a priori. The benefit of this approach is real for practical industrial inspection tasks, where the propagation models could be automatically calibrated. Eventually, we assess the performance of our approach using reduced numbers of measurements acquired on the two plates, and following more realistic robot trajectories. The results illustrate that the proposed approach can recover the plate geometry accurately even with sparse measurements, and outperforms the mapping based on the predetermined propagation model.

In future work, the method shall be integrated within a simultaneous localization a mapping framework, as the sensor positions need to be estimated as well. Also, the hypothesis of rectangular plate geometries shall be relaxed, and more complex wave phenomena such as anisotropic and/or multi-modal propagation, diffraction, or mode conversion are to be integrated in the model. The recovery of the real physical parameters, such as plate thickness, and the mapping of defects shall be investigated to make possible a complete robotic NDT task. Finally, the method shall be tested in more realistic conditions, with a real robotic platform such as a magnetic crawler to acquire the signals.

Declaration of interest

The authors declare that they have no known competing financial interests or personal relationships that could have appeared to influence the work reported in this paper.

References

[1] Bugwright2, autonomous robotic inspection and maintenance on ship hulls and storage tanks, description of the innovative action (Information and communication technologies). (2020).

[2] Roboplanet, robots for human and industrial and safety `http://www.roboplanet.fr/en/`

[3] Su, Z., and Ye, L. (2011). Identification of Damage Using Lamb Waves. In Lecture Notes in Applied and Computational Mechanics: Vol. 56 LNACM.

[4] Zhao, M., Zhou, W., Huang, Y., and Li, H. (2021). Sparse Bayesian learning approach for propagation distance recognition and damage localization in plate-like structures using guided waves. Structural Health Monitoring, 20(1), 3–24. https://doi.org/10.1177/1475921720902277

[5] Z. Su, L. Ye, and Y. Lu, "Guided lamb waves for identification of damage in composite structures: A review,"Journal of Sound and Vibration, vol. 295, no. 3, pp. 753 – 780, 2006.

[6] Hall, J. S., McKeon, P., Satyanarayan, L., Michaels, J. E., Declercq, N. F., and Berthelot, Y. H. (2011). Minimum variance guided wave imaging in a quasi-isotropic composite plate. Smart Materials and Structures, 20(2). https://doi.org/10.1088/0964-1726/20/2/025013

[7] O'Donoughue, N., Harley, J. B., Liu, C., Moura, J. M. F., and Oppenheim, I. (2012). Maximum likelihood defect localization in a pipe using guided acoustic waves. Conference Record - Asilomar Conference on Signals, Systems and Computers, 1863–1867. https://doi.org/10.1109/ACSSC.2012.6489360

15

[8] Anton, S. R., Inman, D. J., and Park, G. (2009). Reference-free damage detection using instantaneous baseline measurements. AIAA Journal, 47(8), 1952–1964. https://doi.org/10.2514/1.43252

[9] Qiu, J., Li, F., Abbas, S., and Zhu, Y. (2019). A baseline-free damage detection approach based on distance compensation of guided waves. Journal of Low Frequency Noise Vibration and Active Control, 38(3–4), 1132–1148. https://doi.org/10.1177/1461348418813699

[10] Lee, S. J., Gandhi, N., Hall, J. S., Michaels, J. E., Xu, B., Michaels, T. E., and Ruzzene, M. (2012). Baseline-free guided wave imaging via adaptive source removal. Structural Health Monitoring, 11(4), 472–481. https://doi.org/10.1177/1475921711435536

[11] Han, J. H., and Kim, Y. J. (2015). Time-frequency beamforming for nondestructive evaluations of plate using ultrasonic Lamb wave. Mechanical Systems and Signal Processing, 54, 336–356. https://doi.org/10.1016/j.ymssp.2014.09.008

[12] Dobie, G., Pierce, S. G., and Hayward, G. (2013). The feasibility of synthetic aperture guided wave imaging to a mobile sensor platform. Ndt & E International, 58, 10-17.

[13] Tabatabaeipour, M. et al. (2019, October). A feasibility study on guided wave-based robotic mapping. In 2019 IEEE International Ultrasonics Symposium (IUS) (pp. 1567-1570). IEEE.

[14] Miranda, A., Gonzales, C., Balyan, A., and Schaal, C. (2019). Mobile robotic platform for inspecting aircraft surfaces using lamb waves. Structural Health Monitoring 2019.

[15] Galán, J. M., and Abascal, R. (2002). Numerical simulation of Lamb wave scattering in semi-infinite plates. International Journal for Numerical Methods in Engineering, 53(5), 1145–1173. https://doi.org/10.1002/nme.331

[16] Ouabi, O., Pomarede, P., Geist, M., Declercq, N. F. and Pradalier, C. (2020). Monte-Carlo Localization on Metal Plates Based on Ultrasonic Guided Waves. The 17th International Symposium on Experimental Robotics, 345–353.

[17] Thrun, S., Wolfram, B., and Fox, D. (2005). Probabilistic Robotics - 2nd edition. In Intelligent Robotics and Autonomous Agents series (MIT Press).

[18] Xu, C., Yang, Z., and Deng, M. (2020). Weighted structured sparse reconstruction-based lamb wave imaging exploiting multipath edge reflections in an isotropic plate. Sensors (Switzerland), 20(12), 1–17. https://doi.org/10.3390/s20123502

[19] Ebrahimkhanlou, A., Dubuc, B., and Salamone, S. (2016). Damage localization in metallic plate structures using edge-reflected lamb waves. Smart Materials and Structures, 25(8). https://doi.org/10.1088/0964-1726/25/8/085035

[20] Zeng, L., Huang, L., Luo, Z., and Lin, J. (2020). Damage imaging that exploits multipath scattered Lamb waves. Structural Health Monitoring, 19(6), 1629–1644. https://doi.org/10.1177/1475921719892828

[21] Hall, J. S. and Michaels, J. E. (2015). Multipath ultrasonic guided wave imaging in complex structures. Structural Health Monitoring, 14(4), 345–358. https://doi.org/10.1177/1475921715578316

[22] Schaal, C., Brown, M., and Schulz, K. (2019). Experimental investigation of Lamb wave-based edge detection methods. 1097223(April 2019), 71. https://doi.org/10.1117/12.2515452

[23] Hong, E., and Schaal, C. (2018). Reverse engineering stiffened plates using guided wave-based nondestructive testing methods. March 2018, 13. https://doi.org/10.1117/12.2296745

[24] Grabowski, K., Gawronski, M., Baran, I., Spychalski, W., Staszewski, W. J., Uhl, T., Kundu, T., and Packo, P. (2016). Time-distance domain transformation for Acoustic Emission source localization in thin metallic plates. Ultrasonics, 68, 142–149. https://doi.org/10.1016/j.ultras.2016.02.015

[25] Sen, N., and Kundu, T. (2020). Acoustic source localization in a highly anisotropic plate with unknown orientation of its axes of symmetry and material properties with numerical verification. Ultrasonics, 100(April 2019), 105977. https://doi.org/10.1016/j.ultras.2019.105977

[26] Miranda, A., Hook, J. Vander, and Schaal, C. (2021). Lamb wave-based mapping of plate structures via frontier exploration. Ultrasonics, 110(September 2020), 106282. https://doi.org/10.1016/j.ultras.2020.106282

[27] Montemerlo, M., Thrun, S., Koller, D., and Wegbreit, B. (2002). FastSLAM: A Factored Solution to the Simultaneous Localization and Mapping Problem Michael. Proceedings of the National Conference on Artificial Intelligence.

[28] Pradalier, C., Ouabi, O. L., Pomarede, P., and Steckel, J. (2020). On-plate localization and mapping for an inspection robot using ultrasonic guided waves: A proof of concept. IEEE International Conference on Intelligent Robots and Systems, 5045–5050. https://doi.org/10.1109/IROS45743.2020.9340936

[29] Van Veen, B. D., and Buckley, K. M. (1988). Beamforming: A Versatile Approach to Spatial Filtering. IEEE ASSP Magazine, 5(2), 4–24. https://doi.org/10.1109/53.665

[30] Ouabi, O. L., Pomarede, P., Geist, M., Declercq, N. F. and Pradalier, C. (2021). A FastSLAM Approach Integrating Beamforming Maps for Ultrasound-based Robotic Inspection of Metal Structures. IEEE Robotics and Automation Letters, 6(2). https://doi.org/10.1109/LRA.2021.3062600

[31] S. Chaabene, F. Bouchoucha, M. N. Ichchou, and M.Haddar (2015). "Wave mode diffusion and propagation in structural wave guide under Varying Temperature". In: Applied Acoustics 108, pp. 84–91.

[32] Zabbal, P., Ribay, G., Chapuis, B., and Jumel, J. (2018). Multichannel Multiple Signal Classification for dispersion curves extraction of ultrasonic guided waves. The Journal of the Acoustical Society of America, 143(2), EL87-EL92.

[33] Chang, C. Y., and Yuan, F. G. (2018). Extraction of guided wave dispersion curve in isotropic and anisotropic materials by Matrix Pencil method. Ultrasonics, 89, 143-154.

[34] Chong, S. Y. and Todd, M. D. (2018). Dispersion curve estimation via a spatial covariance method with ultrasonic wavefield imaging. Ultrasonics, 89, 46-63.

[35] Q. Chen, K. Xu, and D. Ta (2021). High-resolution Lamb waves dispersion curves estimation and elastic property inversion. Ultrasonics, 115, 106427.

[36] Kundu, T., Yang, X., Nakatani, H., and Takeda, N. (2015). A two-step hybrid technique for accurately localizing acoustic source in anisotropic structures without knowing their material properties. Ultrasonics, 56, 271-278.

[37] Yin, S., Cui, Z., and Kundu, T. (2018). Acoustic source localization in anisotropic plates with "Z" shaped sensor clusters. Ultrasonics, 84, 34-37.

[38] Sazontov, A. G., and Malekhanov, A. I. (2015). Matched field signal processing in underwater sound channels (Review). Acoustical Physics, 61(2), 213–230. https://doi.org/10.1134/S1063771015020128

[39] Baggeroer, A. B., and Kuperman, W. A. (1993). Matched Field Processing in Ocean Acoustics. Acoustic Signal Processing for Ocean Exploration, 79–114. https://doi.org/10.1007/978-94-011-1604-6_8

[40] Collins, M. D., and Kuperrnan, W. A. (1991). Focalization: Environmental focusing and source localization. Journal of the Acoustical Society of America, 90(3), 1410–1422. https://doi.org/10.1121/1.401933

[41] Lamb, H. (1917). On waves in an elastic plate. Proceedings of the Royal Society of London. Series A, Containing papers of a mathematical and physical character, 93(648), 114-128.

[42] Kuperman, W. A., Collins, M. D., Perkins, J. S., and Davis, N. R. (1990). Optimal time-domain beamforming with simulated annealing including application of a priori information. Journal of the Acoustical Society of America, 88(4), 1802–1810. https://doi.org/10.1121/1.400201

[43] Liu, Z., and Chen, H. (2018). Application and Challenges of Signal Processing Techniques for Lamb Waves Structural Integrity Evaluation: Part A-Lamb Waves Signals Emitting and Optimization Techniques. Structural Health Monitoring from Sensing to Processing, 32(July), 137–144. https://doi.org/10.5772/intechopen.78381.

[44] Galán, J. M. and Abascal, R. (2002). Numerical simulation of

Lamb wave scattering in semi-infinite plates. International Journal for Numerical Methods in Engineering, 53(5), 1145–1173. https://doi.org/10.1002/nme.331

[45] Huthwaite, P., and Simonetti, F. (2013). High-resolution guided wave tomography. Wave Motion, 50(5), 979–993. https://doi.org/10.1016/j.wavemoti.2013.04.0044

[46] Quaegebeur, N., Masson, P., Langlois-Demers, D., and Micheau, P. (2011). Dispersion-based imaging for structural health monitoring using sparse and compact arrays. Smart Materials and Structures, 20(2). https://doi.org/10.1088/0964-1726/20/2/025005

[47] H. Kuttruff, Room Acoustics, fourth edition, 2000.

[48] Kirkpatrick, S., Gelatt, C. D., and Vecchi, M. P. (1983). Optimization by simulated annealing. Science, 220(4598), 671–680. https://doi.org/10.1126/science.220.4598.671